Journal of
Biomedical Optics

SPIEDigitalLibrary.org/jbo

Artifact reduction method in ultrasound-guided diffuse optical tomography using exogenous contrast agents

Yasaman Ardeshirpour
Nrusingh Biswal
Andres Aguirre
Quing Zhu

SPIE

Journal of Biomedical Optics 16(4), 046015 (April 2011)

Artifact reduction method in ultrasound-guided diffuse optical tomography using exogenous contrast agents

Yasaman Ardeshirpour, Nrusingh Biswal, Andres Aguirre, and Quing Zhu
University of Connecticut, Electrical and Computer Engineering Department, Storrs, Connecticut 06269

Abstract. In diffuse optical tomography (DOT), a typical perturbation approach requires two sets of measurements obtained at the lesion breast (lesion or target site) and a contra-lateral location of the normal breast (reference site) for image reconstruction. For patients who have a small amount of breast tissue, the chest-wall underneath the breast tissue at both sites affects the imaging results. In this group of patients, the perturbation, which is the difference between measurements obtained at the lesion and reference sites, may include the information of background mismatch which can generate artifacts or affect the reconstructed quantitative absorption coefficient of the lesion. Also, for patients who have a single breast due to prior surgery, the contra-lateral reference is not available. To improve the DOT performance or overcome its limitation, we introduced a new method based on an exogenous contrast agent and demonstrate its performance using animal models. Co-registered ultrasound was used to guide the lesion localization. The results have shown that artifacts caused by background mismatch can be reduced significantly by using this new method. [DOI: 10.1117/1.3569088]

Keywords: diffuse optical tomography; exogenous contrast agents; imaging reconstruction.

Paper 10511R received Sep. 16, 2010; revised manuscript received Jan. 29, 2011; accepted for publication Feb. 22, 2011; published online Apr. 21, 2011.

1 Introduction

In the last decade, diffuse optical tomography (DOT) using near-infrared (NIR) light has shown great promise in distinguishing benign from malignant breast tumors and in assessing chemotherapy response of advanced breast cancer.[1–19] In the NIR wavelength range (680 to 900 nm), water absorption is very low and the major endogenous absorbers are oxy- and deoxy-hemoglobin in the blood. This makes the NIR light suitable for detecting tumor hemoglobin concentration and oxygen saturation. Hemoglobin concentration and oxygen saturation are directly related to tumor angiogenesis and tumor hypoxia.[20,21] In addition to the endogenous absorbers, many research groups have developed different exogenous contrast agents to enhance the contrast of the malignant tumors versus normal tissues.[22–26] Currently, indocyanine green (ICG) is the only FDA approved absorption and fluorescent contrast agent in the NIR range. ICG primarily acts as a blood pooling agent in NIR imaging and can provide absorption and fluorescence contrast between a tumor bed and the surrounding normal tissue.[27–42]

In this study, we introduce an ICG-absorption-based optical tomography imaging method for reduction of background artifacts in optical tomography. Co-registered ultrasound was used to assist the localization of the lesion in imaging reconstruction. The study was motivated by solving the problems that the optical tomography community often encounters when imaging breast lesions by using a hand-held probe in reflection geometry and the perturbation approach for image reconstruction.

For tomography reconstruction, the perturbation-based approach requires data from a reference site which should have similar background optical properties as the lesion site for best imaging quality.[43–45] In general, a contra-lateral location at the same quadrant as the lesion is chosen for the reference site. The perturbation is the difference between the measurements obtained at the lesion and the reference sites. This procedure uses the patient's own background tissue optical properties as a control and is thus insensitive to patient's background optical property changes. This can improve the image reconstruction since the data from published literature have shown that breast tissue has a wide range of bulk optical properties that change with age, menopause status, hormone regulation, etc.[1,46]

On the other hand, this procedure is sensitive to contra-lateral site selection. Based on our clinical studies, for patients who have a small amount of breast tissue and a shallower chest-wall, the difference between chest-wall position underneath the breast tissue at both sites affects the imaging results. In this group of patients, the perturbation not only has the information of the lesion, but also contains the information of the difference between the backgrounds at the lesion and reference sites.[43–45] This extra perturbation due to the background mismatch between the lesion and reference sites can cause imaging artifacts and affect the reconstructed absorption coefficient of the lesion.[43,44]

A clinical example is given in Fig. 1 to illustrate the problem of chest-wall effect on optical reflection measurements. Figures 1(a)–1(c) show the co-registered ultrasound (US) images acquired at three different locations of the same quadrant of a 65-year old patient. In these sets of data, the center depth of the breast-tissue and chest-wall interface from a hand-held optical probe of 10 cm diam was moved from 1.2 cm in Fig. 1(a) to 1.5 cm in Fig. 1(b) and 2.2 cm in Fig. 1(c). Figure 1(d) shows the slope of the measured amplitude (logarithmic scale) of the reflection data is different in each case, which is caused by the different chest-wall position and tilting angle. The slope will affect the measured background optical properties.

Address all correspondence to: Quing Zhu, University of Connecticut, ECE, 371 Fairfield Road, U1157, Storrs, Connecticut 06269. Tel: 860 486 5523; Fax: 860 486 2447; E-mail: zhu@engr.uconn.edu.

1083-3668/2011/16(4)/046015/11/$25.00 © 2011 SPIE

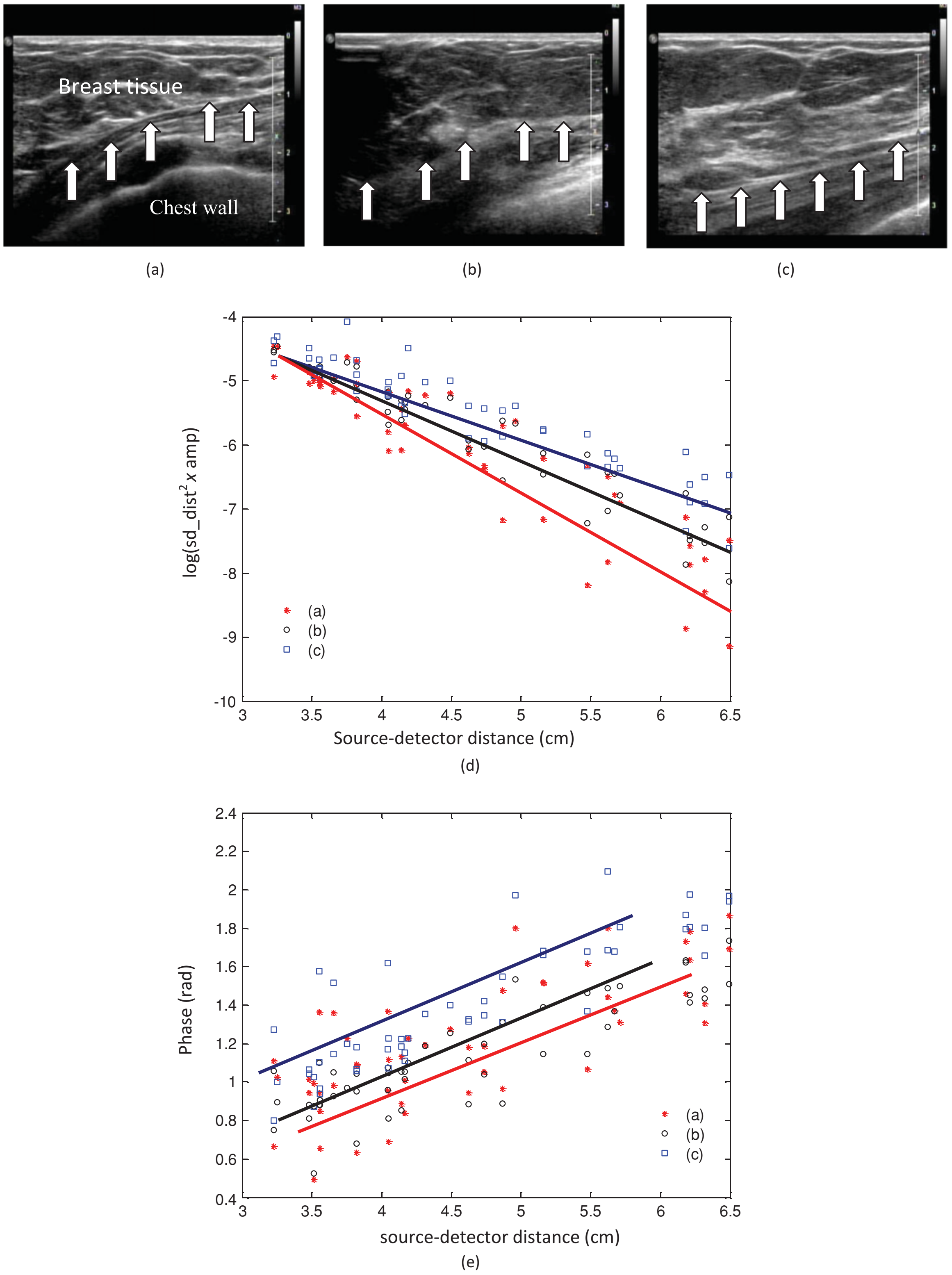

Fig. 1 Co-registered ultrasound images and the light reflectance measurements obtained from a 65 year old patient. (a)–(c) show three images from the breast tissue and chest-wall at different locations with different depth and tilting angle. (d) shows the corresponding light reflectance data (logarithmic scale) versus source-detector distances for (a)–(c). Each line is a fitted curve for each case. (e) shows the phase (rad) versus source-detector distances for (a)–(c).

In Ref. 43 a model-based approach has been introduced to decrease the background artifacts, however, it has limitations. It is computationally intensive and requires a 3D co-registered ultrasound image to model the breast tissue and chest wall as a two-layer medium. The new method introduced in this paper uses an absorption contrast agent which is more robust. This method is also useful for imaging patients who have a single breast due to prior surgery. In this method, the perturbation was defined as the difference between the optical measurements at the lesion site before and after injection of a contrast agent. Since the position of the probe is fixed in both imaging conditions, the breast-tissue and chest-wall background are the same in both sets of data. To the best of our knowledge, this is the first investigation of using an ultrasound-guided, ICG-absorption-based optical tomography method targeted at reducing image artifacts in breast imaging.

The drawback of the correction method is the loss of the lesion hemoglobin contrast in reconstructed absorption images because of the subtraction of the pre-injection data at the same lesion site. However, the ICG absorption is several times higher than that of hemoglobin, therefore, the ICG accumulated in the tumor-bed may be sufficient to distinguish the malignant from benign lesions. This method can be further improved by using exogenous dyes which can bind to specific receptors in the tumor and can be washed out from the background tissue.[22–26]

In this study, phantom and animal studies were conducted to test the performance of this method. Phantom studies were performed using targets of different ICG concentrations and located at different depths. To demonstrate the method in animal studies, we have taken step-by-step approaches using an isolated tumor model from background tissue induced in the mouse foot pad and a tumor model with surrounding background tissue induced in the mouse mammary fat pad.

2 Ultrasound-Guided DOT System

Our US-guided DOT system consisted of four laser diodes of 740, 780, 808, and 830 nm and 14 parallel detectors. Measurements from two wavelengths of 740 and 780 nm were used for this study. The output of each laser diode was modulated at 140 Mhz. Each laser diode was sequentially switched to 9 source positions on the probe and 14 parallel detection channels acquired backscattered light simultaneously for each source position. The ultrasound transducer was positioned in the center of the probe and optical measurements and the ultrasound images were obtained simultaneously. The real-time ultrasound helped to localize the lesion and to improve the light quantification of the lesion by providing the lesion geometry to the optical imaging reconstruction algorithm.[19] Figures 2(a) and 2(b) show the ultrasound and optical source and detector positions on the hand-held probes used in the experiments. More details on our hand-held imaging probe and the NIR system can be found in Ref. 19.

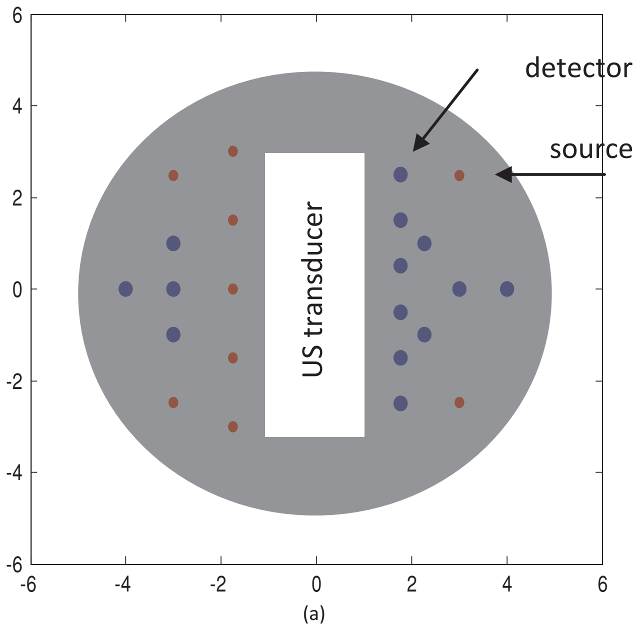

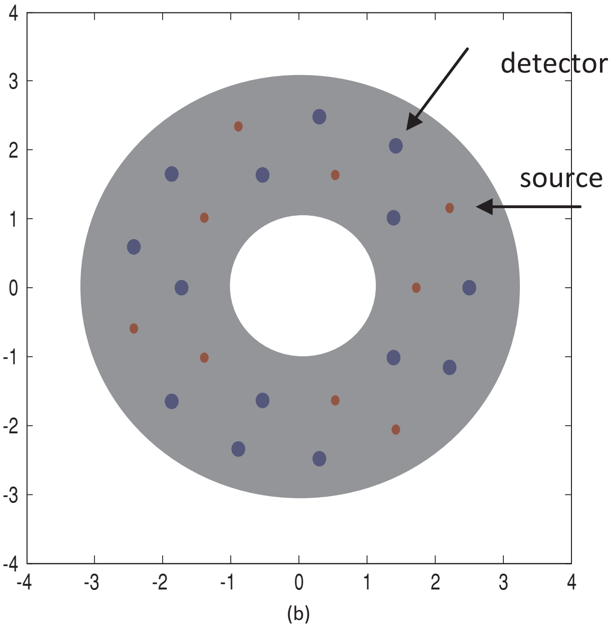

Fig. 2 DOT-US hand-held probe. (a) Probe used in phantom and the first sets of mouse experiments; (b) probe used in the second sets of mouse experiments. Small dots are optical sources and larger dots are optical detectors.

3 Imaging Reconstruction Method

In the proposed imaging method, the lesion is being imaged two times, before and after the injection of the contrast agent (Fig. 3). In both optical images, because the DOT-US probe is fixed at the lesion location, the background (the breast-tissue and chest-wall location) in both sets of data does not change. Therefore, after subtracting the two data sets [Eq. (1)], the information that remains,is the absorption of the contrast agent in the lesion area. In this method, the assumption is that the ICG accumulates in the tumor area and its accumulation in the background is negligible, so the perturbation contains only the information of the lesion.

$$\text{Normalized perturbation} = \frac{U_0\_\text{tar}_{\text{meas}}(\text{ICG}) - U_0\_\text{ref}_{\text{meas}}(\text{no ICG})}{U_0\_\text{ref}_{\text{meas}}(\text{no ICG})} = \frac{U_0\_\text{tar}_{\text{meas}}(\text{ICG})}{U_0\_\text{ref}_{\text{meas}}(\text{no ICG})} - 1, \quad (1)$$

The image reconstructed algorithm has two parts. In the first part, the optical properties of the background are estimated by a fitting algorithm.[19,43] This information is used to calculate the weight matrix more accurately. The second step is the

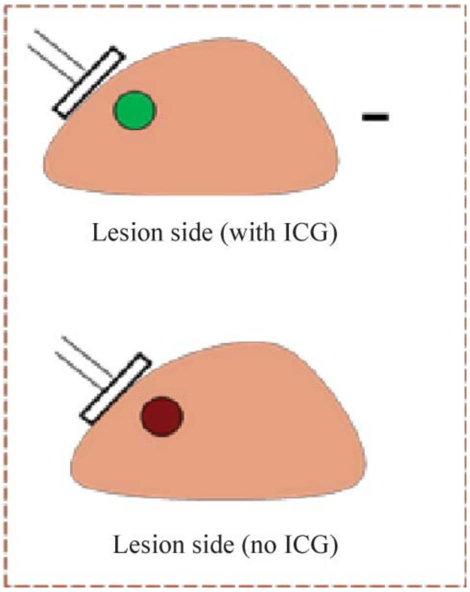

Fig. 3 A schematic of the background-mismatch artifact reduction method using an absorption contrast agent. Two data sets are captured, one before and one after injection of the contrast agent.

reconstruction of the absorption coefficient of the lesion. This part is based on a modified Born approximation and uses the perturbation formula in Eq. (1). To improve the reconstructed target absorption coefficient, a dual-zone mesh scheme with a region of interest identified by co-registered ultrasound is used for the weight matrix calculation.[19] A conjugate gradient method has been used to reconstruct optical absorption properties of targets.

4 Animal Tumor Models

To demonstrate the artifact reduction method step-by-step, we have used two breast cancer cell lines injected at two different locations in the animal studies. In the first experiment, a foot pad tumor model was used to isolate the tumor from the rest part of the body for imaging. The 66c14 cell line is a slow growing mouse mammary carcinoma that does not often exhibit necrosis at the primary site. Five million cells diluted in 20 μl of phosphate buffered saline (PBS) were injected to the right footpad of a 6 week old 20 g female mouse. The second cell line was 4T1 mouse mammary carcinoma, which was an aggressive mouse mammary cell line. 100,000 of cells diluted in 50 μl of PBS were injected to the right mammary fat pad of a 6 week old 18 g female mouse. The mammary fat pad tumor model presents a more challenging imaging scenario because the tumor is closer to other organs where the ICG can accumulate as well. An animal was kept under isoflourine anesthesia after cell line injection for about 30 min to decrease the chance of metastasis of the cancer cells due to movement. The mouse was monitored every day and the imaging started as soon as the tumor grew larger than 0.8 cm. Hair in the tumor areas was removed before imaging.

5 Contrast Agent

ICG is the only FDA approved contrast agent in NIR range. It has been used for ophthalmic retinal angiography[33] and has been widely adopted as a contrast agent in diffused and fluorescence optical tomography.[27–42] In a tumor, blood vessels have larger pores which allow ICG molecules to leak into the extravascular spaces and accumulate in the tumor bed.[25,37] ICG, in general, can bind to the blood plasma protein which can affect its optical properties. On the other hand, ICG has high protein binding. Blood proteins are large molecules and binding to these proteins reduces the leakage of ICG to the tumor vasculatures and causes a fast clearance by liver. This makes the ICG tumor localization poor and unstable after a short period of time.[25,37] An ICG derivative used in this study, referred to as ICG in the following text, was first introduced by Licha et al[37] and has been synthesized by Pavlik et al[38] to reduce its protein binding and to improve its clearance rate from the tumor.[37] The details of the chemical structure and synthesis can be found in Ref. 38.

An example of the measured absorption spectra of ICG obtained in PBS and Dulbecco's modified eagle's medium (DMEM) with 1% and 10% fetal bovine serum (FBS) is shown in Fig. 4. DMEM is the media used for cell culture. As shown in Fig. 4, the ICG absorption coefficient did not show any difference by dissolving it in PBS and DMEM at the wavelengths between 650 to 900 nm. However, the ICG absorption coefficient was increased by adding the FBS which is a blood protein compound. The results show that the ICG absorption increases in the blood protein media and it is expected to be increased in *in vivo* studies. The molar absorption coefficient for ICG derivative is about 200000 (L mol^{-1} cm^{-1}) in PBS and 240000 in 10% FBS. The value is higher than that of commercial ICG which has a molar absorption coefficient of 115000 (L mol^{-1} cm^{-1}) in PBS and 215000 (L mol^{-1} cm^{-1}) in plasma.[37,47] On the other hand, these values show that the optical properties of the ICG derivative are more stable in blood plasma protein compared with that of the commercial ICG. In Ref. 37 the protein binding of the ICG derivative was reported with a reduction to 20% compared to the commercial ICG. This allows the ICG derivative to remain longer than the commercial ICG in the tumor bed during the *in vivo* studies.[37] The peak absorption coefficient of this ICG is at 755 nm. The shift in the absorption coefficient of the ICG derivative compared with the commercial ICG is due to the substitution of the fused benzene rings with carboxylic acid compound.[37]

The absorption coefficient was measured as 81 and 46% of its maximum value (755 nm) at 740 and 780 nm wavelengths which are the wavelengths of the two laser diodes available in our frequency domain system. The measurements from mice tumors and tissue show that the absorption peak has shifted to 780 nm. Therefore, the measurements of phantoms were obtained at 740 nm and tumor imaging data were acquired at 780 nm.

6 Results

6.1 *Phantom Studies*

To obtain a range of detectable ICG concentrations with our DOT system, a 1-cm diameter spherical glass filled with diluted ICG at different concentrations was used. The ICG phantom was placed at 1.5 cm depth from the combined US and DOT probe in 0.8% intralipid solution. In general, 1.5 cm is about

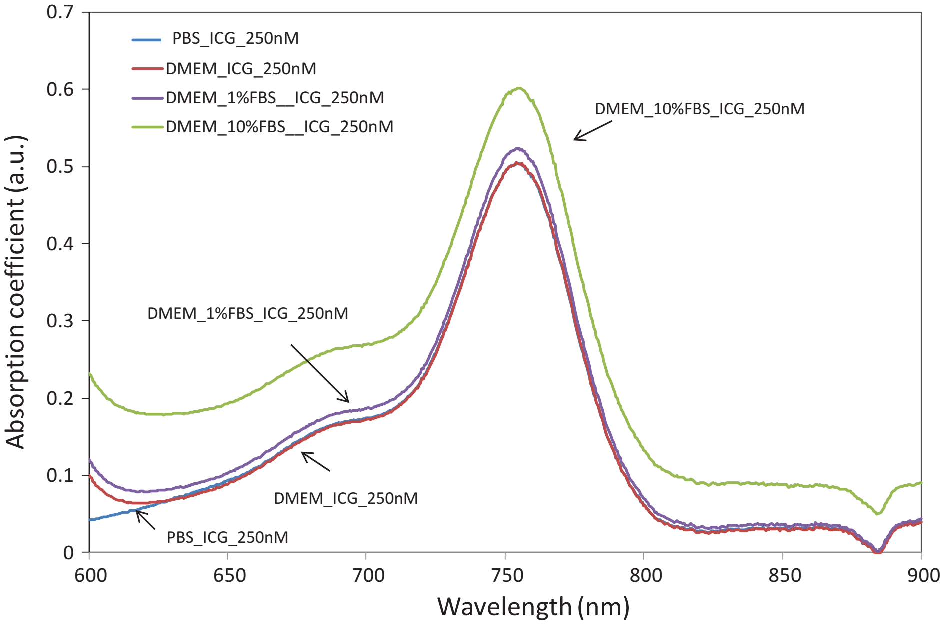

Fig. 4 Measured absorption spectrum of 250 nM ICG in different media. The peak absorption coefficient is at 755 nm. The absorption coefficient drops to 81 and 46% of its maximum value at 740 and 780 nm wavelengths.

the deepest range that we encounter in the chest-wall problems. Beyond 1.5 cm, the chest-wall effect is significantly reduced.[40] The absorption coefficient of the intralipid was measured as $\mu_a = 0.023$ and $\mu_s' = 8\ \text{cm}^{-1}$. The media were imaged twice with and without the ICG phantom. Figure 5 shows the reconstructed image for different ICG concentrations from 940 to 47 nM at 740 nm wavelength. The results show that our DOT system can detect the ICG concentration as low as 50 nM at this depth. Due to the increase of the ICG absorption in blood, we believe that the ICG may be detectable at even lower concentrations in *in vivo* studies.

In the next experiment, a piece of beef rib was located behind the ICG phantom in 0.8% intralipid solution. The beef rib was used to increase the heterogeneity and simulate the imaging condition with the presence of the chest wall. The optical absorption of the beef rib was measured as $\mu_a = 0.1$ and $\mu_s' = 10\ \text{cm}^{-1}$. Figure 6 shows the reconstructed maximum absorption coefficients for different ICG concentrations from 1 μM to 50 nM at 740 nm. Red stars show the calculated true absorption coefficient and blue circles show the measurement values. The results show that the DOT imaging system is capable of detecting the ICG concentration as low as 50 nM under the multilayer and heterogeneous background condition. The error in reconstructed ICG concentrations is less than 20% for 100 nM and higher. However, the error increases for absorptions higher than 0.3 cm^{-1} which is due to the use of linear Born approximation in image reconstruction.[48] The error in reconstructed low ICG concentration of 50 nM is 31%.

To study the effect of target depth on the accuracy of reconstructed concentration, a 1cm ICG phantom with concentration of 1 μM was used. For a better estimate the *in vivo* performance of ICG, 780 nm wavelength was used for this set of experiments. Figure 7 shows the reconstructed concentration with the ICG target located at different depth from 1 to 2.5 cm. The error is less than 5% in the depth range of larger than 1 cm and less than 2.5 cm. The error increases to 22% at depth 1.0 cm and 25% at 2.5 cm. The error in shallow depths (<1 cm) was caused by the lack of source fibers directly located on top of the target because of the need for a co-registered ultrasound transducer in the middle of the combined probe. The error at depths more than 2.5 cm was due to the lower signal-to-noise ratio of the reflectance measurements from deeper targets.

7 Animal Experiments

To estimate the *in vivo* wash in and wash out time, we first conducted a set of monitoring experiments using the mammary fat pad tumor model by placing a source and a detector on top of the tumor with source-detector separation of approximately 1 cm [Fig. 8(a)]. The mouse was anesthetized under isoflurane anesthesia using a nose cone. After capturing several data points, 100 μl of 100 μmol/l of ICG was injected in the tail-vain through a tail vein catheter. The data were captured every 15 s for 45 min after injection. A total of three sets of mice tumors of approximately 9 mm were studied. The half time of the ICG derivative in the normal and tumor area were estimated as 25(+ /–2) and 37(+ /–3) min, respectively, which is almost 5 times higher than the commercial ICG [Fig. 8(b)].[37]

Figure 9 shows a schematic of the animal imaging experimental setup. The mouse was anesthetized and fixed on a transparent plastic sheet. The mouse was partially submerged in the 0.8% intralipid solution and its head stayed outside for breathing under isoflurane anesthesia. A piece of beef rib was placed behind the mouse body to increase the background heterogeneity and to emulate the chest-wall imaging condition. The combined US-DOT probe was submerged in the intralipid tank to image the tumor.

In the first set of the imaging experiments, the foot pad tumor model was used. After the tumor reached a certain size of approximately 7 to 8 mm in about two weeks, the mouse

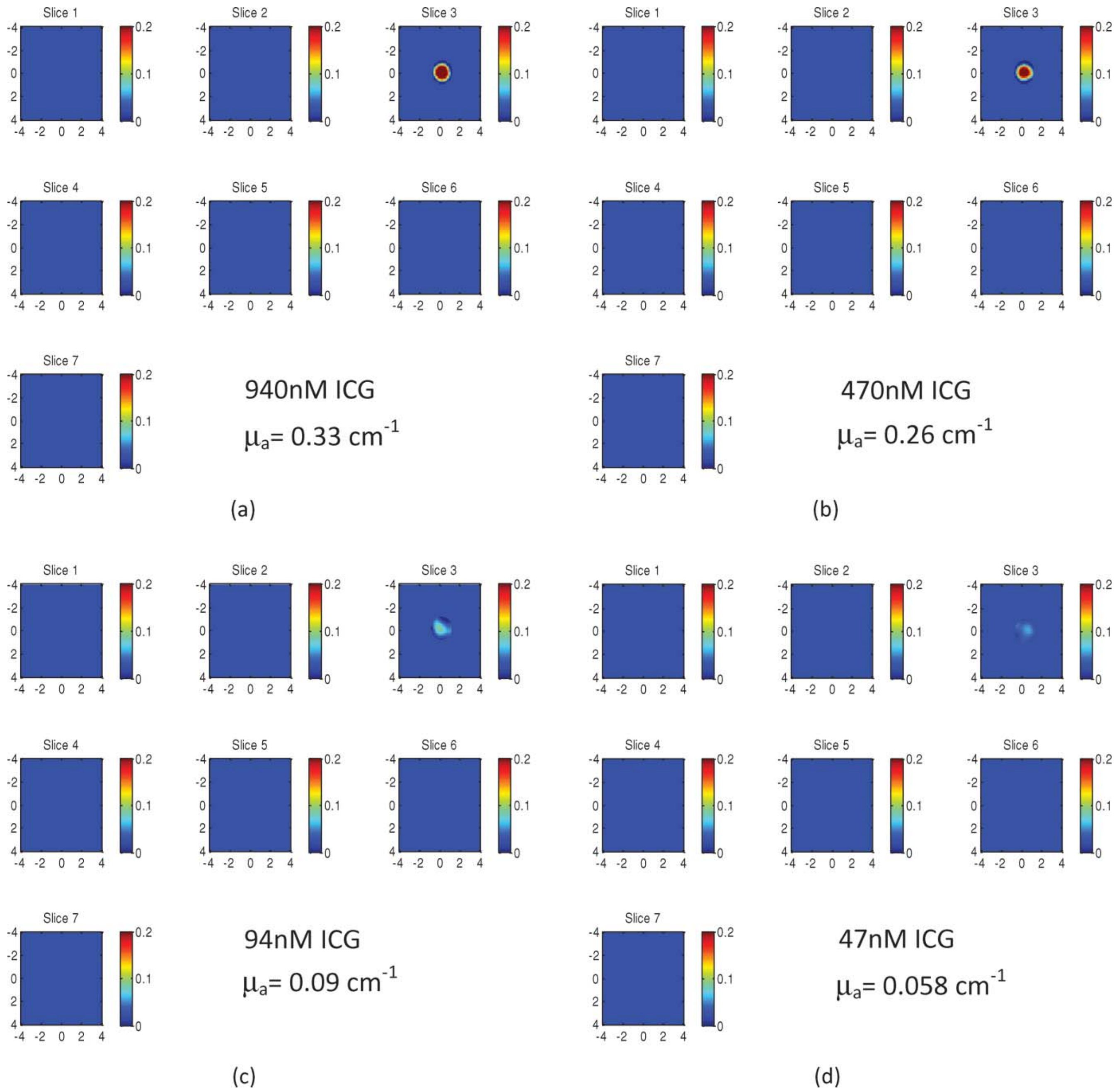

Fig. 5 Reconstructed image of a 1-cm diameter ICG target of concentrations from 1 μM to 50 nM located at 1.5-cm depth from the probe in 0.8% intralipid solution. These data were obtained at 740 nm wavelength. In the absorption map, each slice presents a spatial image of 8 cm × 8 cm obtained from 0.5 cm underneath the probe surface to 3.5 cm in depth with 0.5 cm spacing between slices.

was imaged under isoflurane anesthesia. A piece of pork rib was placed behind the mouse foot to increase the background heterogeneity and emulate the chest-wall. A small mouse pedal catheter (BFL-27–20-B26, Strategic Applications Incorporated, Libertyville, Illinois) was placed in the right footpad, for contrast agent injection during experiment. Because the injection was at the footpad, the ICG was accumulated at the tumor site which was a simplified model to evaluate the correction method.

After taking one set of data, 20 μl ICG with concentration of 50 μmol/l was injected in the right foot-pad. Ultrasound images and optical data from 9 sources and 14 detectors were captured every 1 min. The results are shown in Fig. 10. Figure 10(a) shows the co-registered ultrasound image of the tumor area marked by an arrow. Figure 10(b) shows reconstructed absorption coefficient of the background pork rib inside the intralipid solution. Figures 10(c) and 10(d) show the reconstructed absorption coefficient of the mouse body plus the pork rib immersed inside the intralipid solution before injection and 15 min after injection, respectively. This is the time that the uptake of the ICG was maximum (Fig. 8). Figure 10(e) is the reconstructed absorption coefficient of the target by applying the correction method [Eq. (1)] after the injection of ICG. The reconstructed image of the lesion was at the correct location and a good separation of

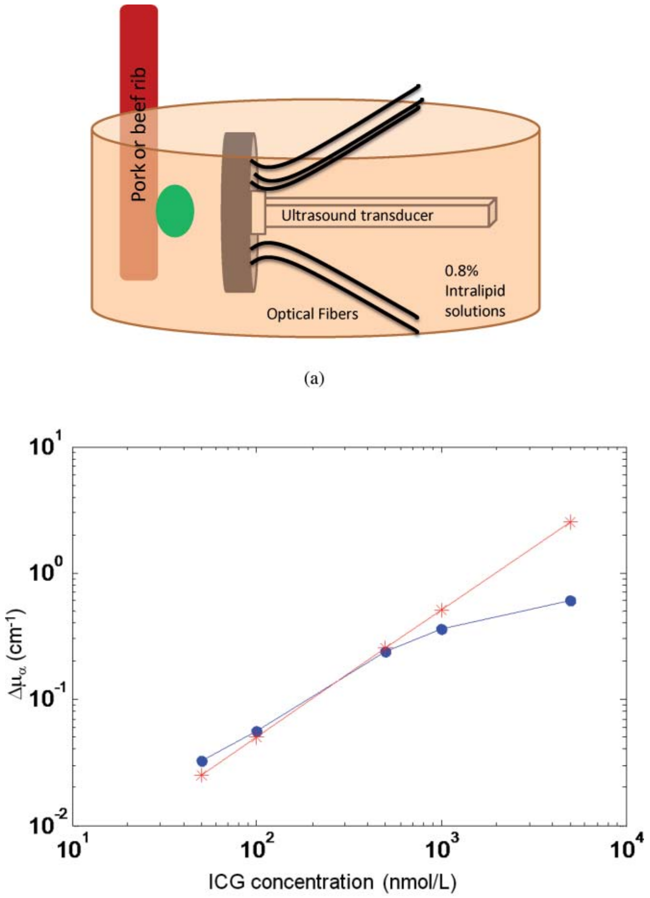

(a)

(b)

Fig. 6 (a) Experimental setup, (b) reconstructed maximum absorption coefficient of an ICG phantom located at 1.5 cm depth from the probe. To increase the heterogeneity of background and emulate the chest-wall effect, a layer of beef rib was placed behind the ICG phantom at 2 cm depth from the probe. The ICG phantom is a 1-cm diameter spherical glass filled with diluted ICG with different concentrations. These data were obtained at 740 nm wavelength. Red stars show the true absorption coefficients and blue circles demonstrate the reconstructed values.

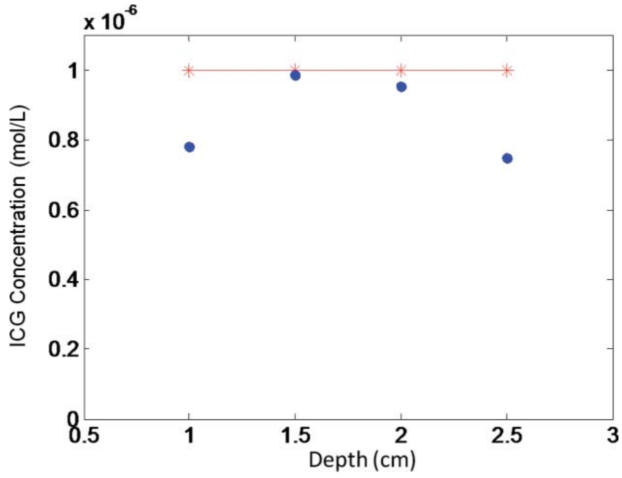

Fig. 7 Reconstructed ICG concentration of an ICG phantom located at different depths from the probe. The ICG phantom is a 1 cm diameter spherical glass filled with 1 μM ICG. These data were obtained at 780 nm wavelength. Red stars show the true concentrations and blue circles demonstrate the reconstructed values.

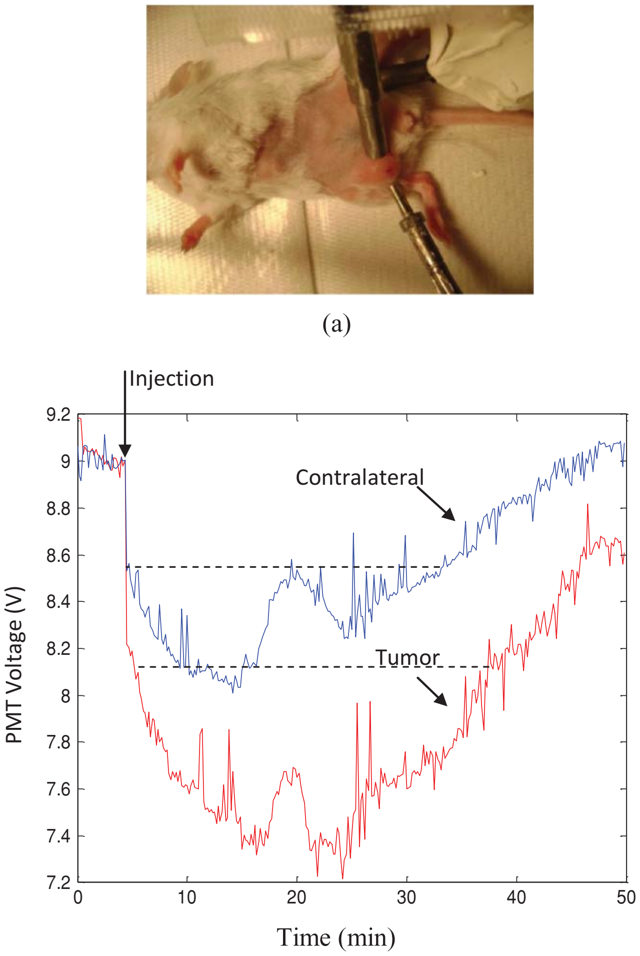

(a)

(b)

Fig. 8 (a) Experimental setup. (b) Time profile of the ICG absorption in the normal contra-lateral site and the tumor area, *y*-axis shows the measured reflectance and *x*-axis shows the time.

the tumor from the background (mouse body and pork rib) was achieved.

To further challenge the correction method, the mammary fat-pad tumor model was used. For this set of experiments, because the distance of the mouse head to the tumor was limited to about 3 to 4 cm, a smaller optical probe, shown in

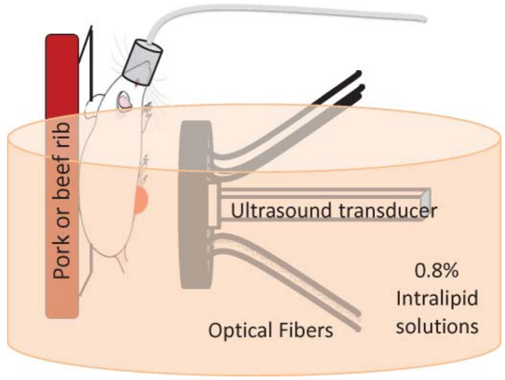

Fig. 9 *In vivo* experimental setup.

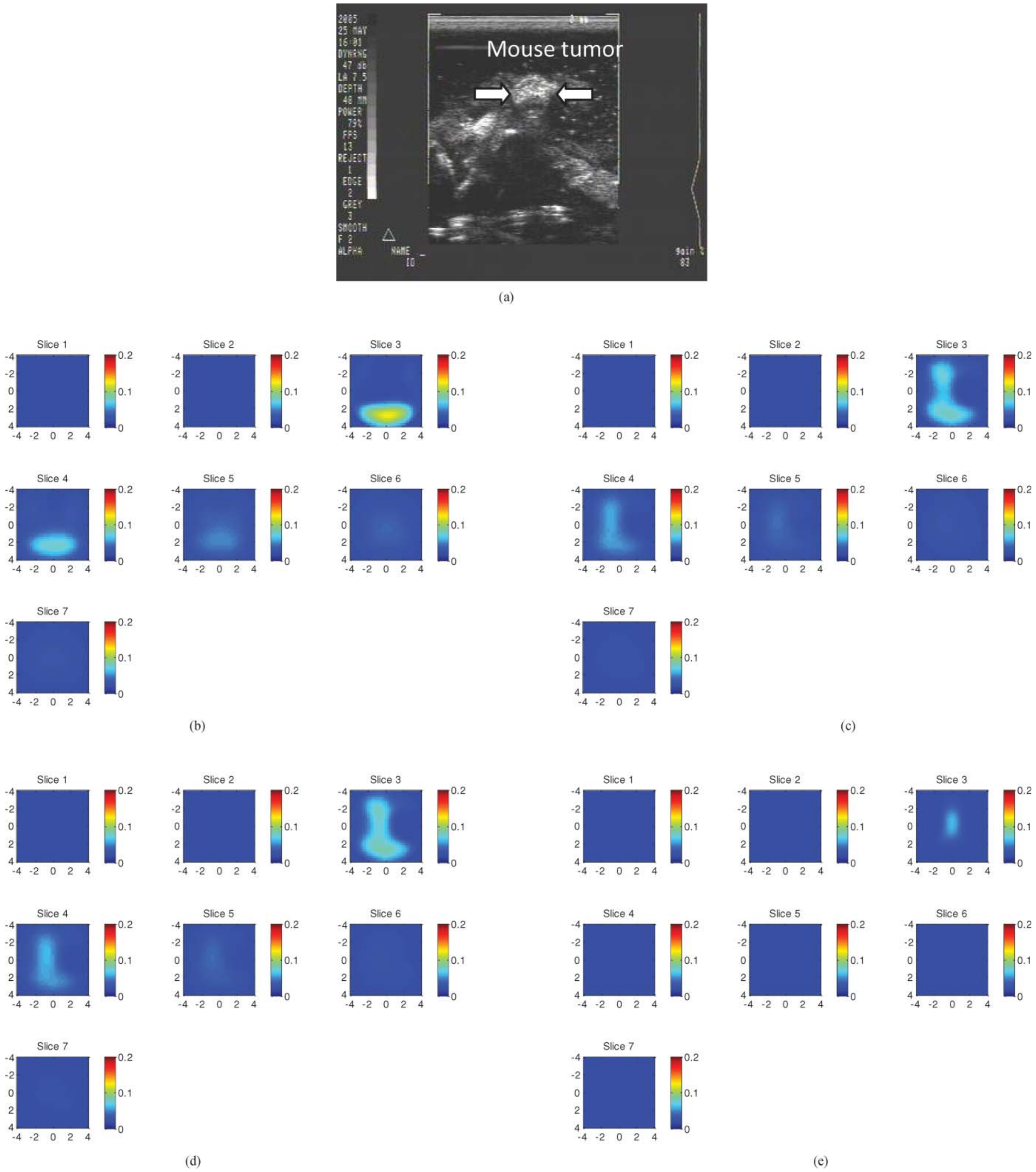

(a)

(b)

(c)

(d)

(e)

Fig. 10 (a) The ultrasound image of the mouse and a layer of a pork rib. The tumor is marked by an arrow. Reconstructed absorption coefficient of (b) the pork rib alone before injection, (c) pork rib and the mouse body before injection, (d) 15 min after injection of 20 μl of 50 μmol/l ICG in the foot-pad, and (e) tumor after subtracting the background. In the absorption map, each slice presents a spatial image of 8 cm × 8 cm obtained from 0.5 cm underneath the probe surface to 3.5 cm in depth with 0.5 cm spacing between slices.

Fig. 2(b), was used. In this probe, the maximum source-detector distance was about 5 cm. The intralipid was heated to the body temperature (about 37°C). A tail-vein catheter with stylette (MTV-01, Strategic Applications Incorporated, Libertyville, Illinois) was used for tail vein injection during experiment. After capturing several sets of ultrasound and optical images with 1 min time separation, 100 μl of 100 μmol/l of ICG was injected through the catheter. The mouse was continuously imaged every 1 min after injection. Figure 11 shows the experimental results. Figure 11(a) shows the co-registered ultrasound image of the

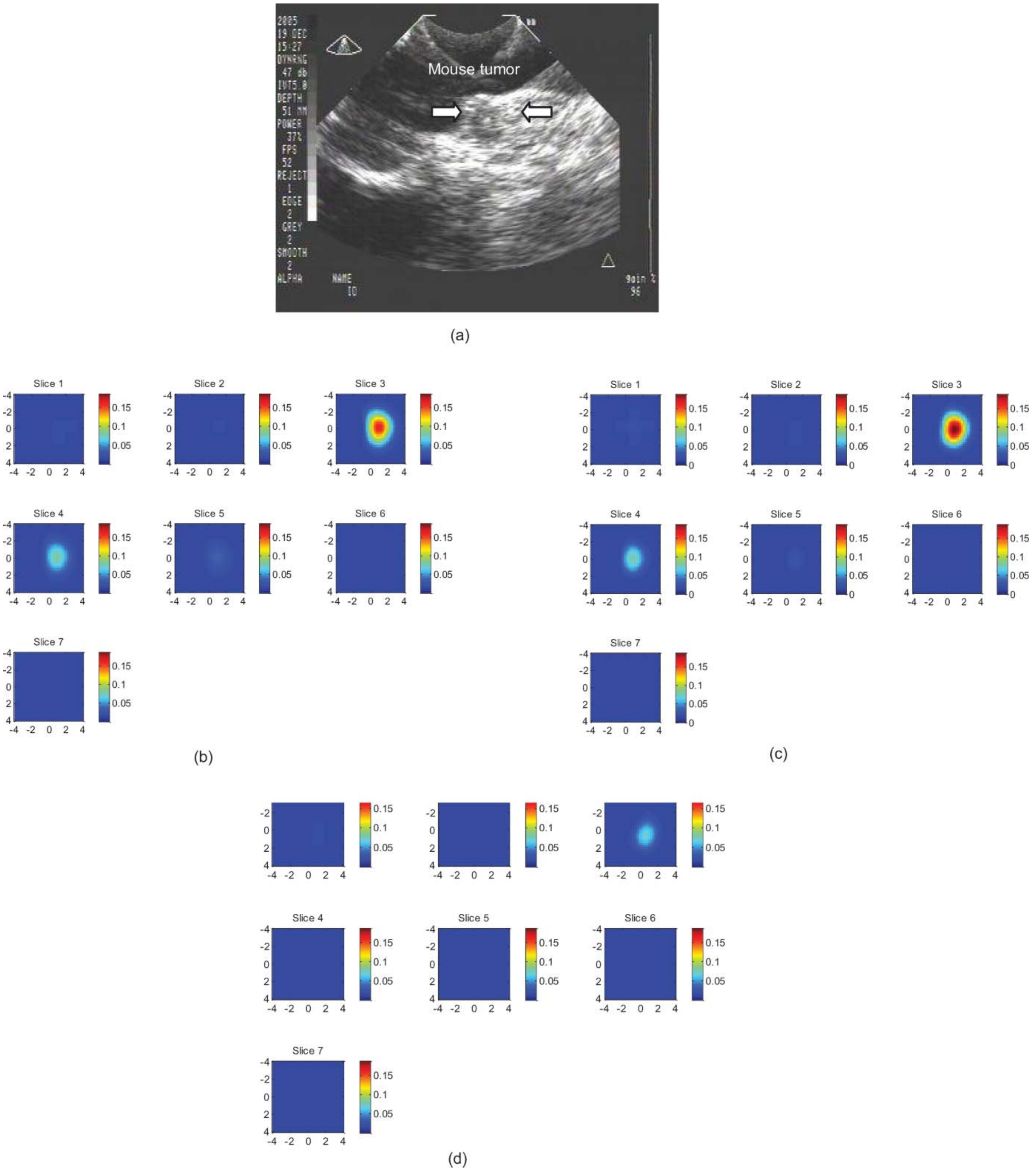

Fig. 11 (a) The ultrasound image of the mouse and a layer of a beef rib. The tumor is marked by an arrow. Reconstructed absorption coefficient of (b) the mouse body and the beef rib before injection, (c) ICG, the mouse body and beef rib 12 min after injection, and (d) ICG after background subtraction, 12 min after.

mouse and a layer of a beef rib behind it. The tumor is marked by an arrow. Figures 11(b) and 11(c) show the reconstructed absorption map of the mouse body and the beef rib before injection [Fig. 11(b)], and 12 min after injection [Fig. 11(c)]. This is almost the time that the uptake of the ICG was maximum (Fig. 8).

Figure 11(d) is the reconstructed absorption coefficient of the ICG injected in the tail-vein after applying the correction method. The lesion appeared at the correct location with good isolation from the background (mouse body and beef rib).

8 Summary and Discussion

In this paper, a background mismatch correction method using an exogenous contrast agent has been introduced and its performance was demonstrated using animal models. The results have shown that this method can significantly reduce artifacts generated by the background mismatch. We believe that the results would be much better in clinical studies because the mouse body is very small and it has much higher heterogeneity than human breast tissue due to the other organs in the field of imaging.

In this paper we used ultrasound-guidance to provide target depth and target location in both phantom and animal studies. Using *a priori* anatomical information of the target can improve the accuracy of the reconstructed absorption values.[49–53] The phantom studies have shown that the reconstruction accuracy is in general within 20% of the calibrated values. This shows dramatic improvement over the methods that use unguided methods with post- and pre-contrast subtraction only. The larger error that occurred in absorption higher than 0.3 cm^{-1} is due to the use of born approximation in high absorption range.

One drawback of using the correction method is the loss of the lesion hemoglobin contrast in reconstructed absorption images because of the subtraction of the post-injected data from pre-injection ones at the same lesion site. However, the ICG absorption is several times higher than that of hemoglobin, therefore, the ICG accumulated in the tumor-bed may be sufficient to distinguish the malignant from benign lesions. In addition, ICG fluorescence properties could be used to further enhance the lesion detection and diagnosis. A recent study in breast cancer clinical report shows two-to-four-fold higher ICG (exogenous contrast agent) fluorescence signals measured in the tumor area compared with total hemoglobin (endogenous contrast agent) due to the tumor vasculature.[40] Therefore, the correction method reported in this paper has a potential to significantly improve the diagnosis of malignant versus benign lesions[32] while reducing the background artifacts in a certain patient population.

Another drawback of using correction method in vivo is the reduction of tumor contrast due to the background ICG uptake. However, as shown in Fig. 8, the tumor uptake is about two times higher than that of background uptake, therefore, a good tumor contrast is obtainable using the correction method.

The reported background mismatch correction method was demonstrated using the ICG derivative synthesized by Pavlik et al.[38] However, this method is not limited to the ICG and its derivatives and can be readily used when other exogenous agents are available for human use. Recently, many nontargeted exogenous contrast agents that have a high absorption coefficient, such as gold nanoparticles or carbon nanotubes,[26] or targeted contrast agents conjugated to the receptors of tumor cells,[22–25] have been synthesized and evaluated in animals. Furthermore, the technique is not limited to correct background mismatch artifacts in breast imaging and can be readily used in other applications where background mismatch has to be removed for improving imaging quality.

Acknowledgments

The authors thank the funding support of this work from the National Institute of Health (R01EB002136) and the Donaghue Medical Research Foundation. The authors thank Professor Michael B. Smith and graduate student Christopher Pavlik at Chemistry Department of University of Connecticut for providing the ICG derivative to this study.

References

1. B. J. Tromberg, A. Cerussi, N. Shah, M. Compton, A. Durkin, D. Hsiang, J. Butler, and R. Mehta, "Diffuse optics in breast cancer: detecting tumors in pre-menopausal women and monitoring neoadjuvant chemotherapy," *Breast Cancer Res.* **7**(6), 279–285 (2005).
2. D. R. Leff, O. J. Warren, L. C. Enfield, A. Gibson, T. Athanasiou, D. K. Patten, J. Hebden, G. Z. Yang, and A. Darzi, "Diffuse optical imaging of the healthy and diseased breast: A systematic review," *Breast Cancer Res.* **108**(1), 9–22 (2008).
3. B. Chance, S. Nioka, J. Zhang, E. F. Conant, E. Hwang, S. Briest, S. G. Orel, M. D. Schnall, and B. J. Czerniecki, "Breast cancer detection based on incremental biochemical and physiological properties of breast cancers: A six-year, two-site study," *Acad. Radiol.* **12**(8), 925–933 (2005).
4. S. P. Poplack, T. D. Tosteson, W. A. Wells, B. W. Pogue, P. M. Meaney, A. Hartov, C. A. Kogel, S. K. Soho, J. J. Gibson and, K. D. Paulsen, "Electromagnetic breast imaging: Results of a pilot study in women with abnormal mammograms," *Radiology* **243**(2), 350–359 (2007).
5. R. Choe, A. Corlu, K. Lee, T. Durduran, S. D. Konecky, M. Grosicka-Koptyra, S. R. Arridge, B. J. Czerniecki, D. L. Fraker, A. DeMichele, B. Chance, M. A. Rosen, and A. G. Yodh, "Diffuse optical tomography of breast cancer during neoadjuvant chemotherapy: A case study with comparison to MRI," *Med. Phys.* **32**(4), 1128–1139 (2005).
6. E. Heffer, V. Pera, O. Schutz, H. Siebold, and S. Fantini, "Near-infrared imaging of the human breast: complementing hemoglobin concentration maps with oxygenation images," *J. Biomed. Opt.* **9**(6), 1152–1160 (2004).
7. X. P. Liang, Q. Z. Zhang, C. Q. Li, S. R. Grobmyer, L. L. Fajardo, and H. B. Jiang, "Phase-contrast diffuse optical tomography: Pilot results in the breast," *Acad. Radiol.* **15**(7), 859–866 (2008).
8. X. Intes, "Time-domain optical mammography SoftScan: Initial results," *Acad. Radiol.* **12**(8), 934–947 (2005).
9. L. Spinelli, A. Torricelli, A. Pifferi, P. Taroni, G. Danesini, and R. Cubeddu, "Characterization of female breast lesions from multi-wavelength time-resolved optical mammography," *Phys. Med. Biol.* **50**(11), 2489–2502 (2005).
10. C. H. Schmitz, D. P. Klemer, R. Hardin, M. S. Katz, Y. L. Pei, H. L. Graber, M. B. Levin, R. D. Levina, N. A. Franco, W. B. Solomon, and R. L. Barbour, "Design and implementation of dynamic near-infrared optical tomographic imaging instrumentation for simultaneous dual-breast measurements,"*Appl. Opt.* **44**(11), 2140–2153 (2005).
11. A. Alexandrakis, T. J. Farrell, and M. S. Patterson, "Accuracy of the diffusion approximation in determining the optical properties of a two-layer turbid medium," *Appl. Opt.* **37**(31), 7401–7409 (1998).
12. D. Floery, T. H. Helbich, C. C. Riedl, S. Jaromi, M. Weber, S. Leodolter, and M. H. Fuchsjaeger, "Characterization of benign and malignant breast lesions with computed tomographic laser mammography (CTLM)," *Invest. Radiol.* **40**, 328–335 (2005).
13. D. Grosenick, K. T. Moesta, M. Moller, J. Mucke, H. Wabnitz, B. Gebauer, C. Stroszczynski, B. Wassermann, P. M. Schlag, and H. Rinneberg, "Time-domain scanning optical mammography: I. Recording and assessment of mammograms of 154 patients," *Phys. Med. Biol.* **50**(11), 2429–2449 (2005).
14. B. Brooksby, B. W. Pogue, S. D. Jiang, H. Dehghani, S. Srinivasan, C. Kogel, T. D. Tosteson, J. Weaver, S. P. Poplack, and K. D. Paulsen, "Imaging breast adipose and fibroglandular tissue molecular signatures by using hybrid MRI-guided near-infrared spectral tomography," *Proc. Natl. Acad. Sci. U.S.A.* **103**(23), 8828–8833 (2006).
15. V. Ntziachristos, A. G. Yodh, M. D. Schnall, and B. Chance, "MRI-guided diffuse optical spectroscopy of malignant and benign breast lesions," *Neoplasia* **4**(4), 347–354 (2002).

16. Q. Zhang, T. J. Brukilacchio, A. Li, J. J. Stott, T. Chaves, E. Hillman, T. Wu, M. Chorlton, E. Rafferty, R. H. Moore, D. B. Kopans, and D. A. Boas, "Coregistered tomographic x-ray and optical breast imaging: initial results," *J. Biomed. Opt.* **10**(2), 024033 (2005).
17. Q. Zhu, M. M. Huang, N. G. Chen, K. Zarfos, B. Jagjivan, M. Kane, P. Hedge, and S. H. Kurtzman, "Ultrasound-guided optical tomographic imaging of malignant and benign breast lesions: Initial clinical results of 19 cases," *Neoplasia* **5**(5), 379–388 (2003).
18. Q. Zhu, E. B. Cronin, A. A. Currier, H. S. Vine, M. M. Huang, N. G. Chen, and C. Xu, "Benign versus malignant breast masses: Optical differentiation with US-guided optical imaging reconstruction," *Radiology* **237**(1), 57–66 (2005).
19. Q. Zhu, C. Xu, P. Guo, A. Aguirre, B. Yuan, F. Huang, D. Castilo, J. Gamelin, S. Tannenbaum, M. Kane, P. Hegde, and S. Kurtzman, "Optimal probing of optical contrast of breast lesions of different size located at different depths by US localization," *Technol. Cancer Res. Treat.* **5**(4), 365–380 (2006).
20. B. W. Pogue, S. P. Poplack, T. O. McBride, W. A. Wells, K. S. Osterman, U. L. Osterberg, and K. D. Paulsen, "Quantitative hemoglobin tomography with diffuse near-infrared spectroscopy: Pilot results in the breast," *Radiology* **218**(1), 261–266 (2001).
21. P. Vaupel and L. Harrison, "Tumor Hypoxia: Causative Factors, Compensatory Mechanisms, and Cellular Response," *Oncologist* **9**(5), 4–9 (2004).
22. C. Bremer, V. Ntziachristos, and R. Weissleder, "Optical-based molecular imaging: contrast agents and potential medical applications," *Eur. J. Radiol.* **13**(2), 231–243 (2003).
23. S. Dufort, L. Sancey, C. Wenk, V. Josserand, and J. L. Coll, "Optical small animal imaging in the drug discovery process," *Biochimica et Biophysica Acta-Biomembranes* **1798**(12), 2266–2273 (2010).
24. K. Licha and C. Olbrich, "Optical imaging in drug discovery and diagnostic applications," *Adv. Drug Delivery Rev*. **57**(8), 1087–1108 (2005).
25. J. V. Frangioni, "In vivo near-infrared fluorescence imaging," *Curr. Opin. Chem. Biol.* **7**(5), 626–634 (2003).
26. A. G. Zuenca, H. B. Jiang, S. N. Hochwald, M. Delano, W. G. Cance, and S. R. Grobmyer, "Emerging implications of nanotechnology on cancer diagnostics and therapeutics," *Cancer* **107**(3), 459–466 (2006).
27. B. Alacam, B. Yazici, X. Intes, S. Nioka, and B. Chance, "Pharmacokinetic-rate images of indocyanine green for breast tumors using near-infrared optical methods," *Phys. Med. Biol*. **53**(4), 837–59 (2008).
28. E. M. C. Hillman and A. Moore, "All-optical anatomical co-registration for molecular imaging of small animals using dynamic contrast," *Nature Photonics* **1**(9), 526–530 (2007).
29. B. W. Pogue, "Near-infrared characterization of disease via vascular permeability probes," *Acad. Radiol.* **13**(1), 1–3 (2006).
30. D. Thayer, M. B. Unlu, Y. Lin, K. Yan, O. Nalcioglu, and G. Gulsen, "Dual-contrast dynamic MRI-DOT for small animal imaging," *Technol. Cancer Res. Treat.* **9**(1), 61–69 (2010).
31. M. B. Unlu, Y. Lin, O. Birgul, O. Nalcioglu, and G. Gulsen, "Simultaneous in vivo dynamic magnetic resonance-diffuse optical tomography for small animal imaging," *J Biomed. Opt.* **13**(6), 060501 (2008).
32. D. J. Cuccia, F. Bevilacqua, A. J. Durkin, S. Merritt, B. J. Tromberg, G. Gulsen, H. Yu, J. Wang, and O. Nalcioglu, "In vivo quantification of optical contrast agent dynamics in rat tumors by use of diffuse optical spectroscopy with magnetic resonance imaging coregistration," *Appl. Opt.* 42(16), 2940–2950 (2003).
33. K. Kogure, N. J. David, U. Yamanouchi, and E. Choromokos, "Infrared absorption angiography of the fundus circulation," *Arch Ophthalmol.* **83**(2), 209–214 (1970).
34. R. C. Benson and H. A. Kues, "Fluorescence properties of indocyanine green as related to angiography," *Phys. Med. Biol.* **23**, 159–163 (1978).
35. M. L. Landsman, G. Kwant, G. A. Mook and W. G. Zijlstra, "Light-absorbing properties, stability, and spectral stabilization of indocyanine green," *J. Appl. Physiol.* **40**(4), 575–583 (1976).
36. V. Ntziachristos, C. Bremer, C. Tung, and R. Weissleder, "Imaging cathepsin B upregulation in HT-1080 tumor models using fluorescence-mediated molecular tomography," *Acad. Radiol.* **9**(2), S323–S325 (2002).
37. K. Licha, B. Riefke, V. Ntziachristos, A. Becker, B. Chance, and W. Semmler, "Hydrophilic cyanine dyes as contrast agents for near-infrared tumor imaging: Synthesis, photophysical properties and spectroscopic in vivo characterization," *Photochem. Photobiol.* **72**(3), 392–398 (2000).
38. C. Pavlik, N. Biswal, F. C. Gaenzler, M. D. Morton, L. T. Kuhn, K. P. Claffey, Q. Zhu, and M. B. Smith, "Synthesis and Fluorescent Characteristics of Imidazole- Indocyanine Green Conjugates Dyes and Pigments," *Dyes Pigm*. **89**(1), 9–15 (2011).
39. V. Ntziachristos, A. G. Yodh, M. Schnall, and B. Chance, "Concurrent MRI and diffuse optical tomography of breast after indocyanine green enhancement," *Proc. Natl. Acad. Sci. U.S.A.* **97**, 2767–2772 (2000).
40. A. Corlu, R. Choe, T. Durduran, M. A. Rosen, M. Shweiger, S. R. Arridge, M. D. Schnall, and A. J. Yodh, "Three-dimensional in vivo fluorescence diffuse optical tomography of breast cancer in humans," *Opt. Express* **15**(11), 6696–6716 (2007).
41. X. Intes, J. Ripoll, Y. Chen, S. Nioka, A. G. Yodh and B. Chance, "In vivo continuous-wave optical breast imaging enhanced with Indocyanine Green," *Med. Phys.* **30**, 1039–1047 (2003).
42. M. Gurfinkel, S. Ke, X. Wen, C. Li, and E. M. Sevick-Muraca, "Near-infrared fluorescence optical imaging and tomography," *Dis. Markers* **19**(2–3), 107–121 (2004).
43. Y. Ardeshirpour, M. Huang, and Q. Zhu, "Effect of chest wall on breast lesion reconstruction," *J. Biomed. Opt.* **14**(4), 041515 (2009).
44. Y. Ardeshirpour and Q. Zhu, "An optical tomography method that accounts for the tilted chest wall in breast imaging," *J. Biomed. Opt.* **15**(4), 044005 (2010).
45. Y. Ardeshirpour, M. Huang, and Q. Zhu, "An optical tomography method that accounts for a tilted chest-wall in breast imaging," *Proceedings of SPIE BIOS*, San Jose, CA (2009).
46. B. W. Pogue, S. Jiang, H. Dehghani, C. Kogel, S. Soho, S. Srinivasan, X. Song, T. D. Tosteson, S. P. Poplack, and K. D. Paulsen, "Characterization of hemoglobin, water, and NIR scattering in breast tissue: analysis of intersubject variability and menstrual cycle changes," *J. Biomed. Opt.* **9**(3), 541–552, (2004).
47. http://www.sigmaaldrich.com/etc/medialib/docs/Sigma/Product_Information_Sheet/2/i2633pis.Par.0001.File.tmp/i2633pis.pdf
48. D. A. Boas, "A fundamental limitation of linearized algorithms for diffuse optical tomography," *Opt. Express* **1**(13), 404–413 (1997).
49. P. K. Yalavarthy, B. W. Pogue, H. Dehghani, C. M. Carpenter, S. Jiang, and K. D. Paulsen, "Structural information within regularization matrices improves near infrared diffuse optical tomography," *Opt. Express* **15**(13), 8043–8058 (2007).
50. Y. Lin, H. Gao, O. Nalcioglu, and G. Gulsen, "Fluorescence diffuse optical tomography with functional and anatomical a priori information: feasibility study," *Phys. Med. Biol.* **52**(18), 5569 (2007).
51. B. A. Brooksby, H. Dehghani, B. W. Pogue, and K. D. Paulsend, "Near-infrared (NIR) tomography breast image reconstruction with a priori structural information from MRI: Algorithm development for reconstructing heterogeneities," *IEEE J. Sel. Top. Quantum Electron*. **9**(2), 199–209(2003).
52. M. Guven, B. Yazici, X. Intes, and B. Chance, "Diffuse optical tomography with a priori anatomical information," *Med. Biol.*," **50**(12), 2837–2858 (2005).
53. N. G. Chen, P. Y. Guo, S. K. Yan, D. Q. Piao, and Q. Zhu, "Simultaneous near infrared diffusive light and ultrasound imaging," *Appl. Opt.* **40**(34), 6367–6380 (2001).